Anisotropic magnetic properties of antiferromagnetic $DyCoGa_5$

Baopeng Song,[1] Zhaoyang Shan,[2] Rui Shi,[1] Sai Yang,[1] Rui Li,[2] Jiahua Min,[1] Zhen Ma,[1] Shuhan Zheng,[1] Meifeng Liu,[1] Xiuzhang Wang,[1] Saiyu Wang,[1] Yongjun Zhang,[1,*] Michael Smidman,[2,†] and Huiqiu Yuan[2,1,3,‡]

[1]*Hubei Key Laboratory of Photoelectric Materials and Devices, School of Materials Science and Engineering, Hubei Normal University, Huangshi 435002, China*

[2]*Center for Correlated Matter and School of Physics, Zhejiang University, Hangzhou 310058, China*

[3]*State Key Laboratory of Silicon Materials, Zhejiang University, Hangzhou 310058, China*

(Received 17 August 2023; revised 5 February 2024; accepted 2 April 2024; published 19 April 2024)

We report a detailed study of the physical properties of single crystals of $DyCoGa_5$ using magnetic susceptibility, specific heat, and resistivity measurements. $DyCoGa_5$ crystallizes in the layered tetragonal $HoCoGa_5$-type structure and undergoes two successive antiferromagnetic transitions at $T_{N1} = 24.7$ K and $T_{N2} = 22.9$ K, which are associated with ordering of the Dy^{3+} moments. We characterize the temperature-field phase diagrams of $DyCoGa_5$ for fields both along the c axis and within the ab plane, where highly anisotropic magnetic behaviors are observed. When fields are applied along the easy c axis, both T_{N1} and T_{N2} are suppressed with increasing field, and multiple metamagnetic transitions are observed, while these transitions exhibit only a weak field dependence for $H \parallel ab$. From our analysis we propose a crystalline-electric-field scheme that gives rise to the observed Ising anisotropy, and a simple model of the magnetic exchange interactions can account for the low-temperature antiferromagnetic phase, as well as the field-induced phase with a magnetization half the saturated value.

DOI: 10.1103/PhysRevB.109.134429

I. INTRODUCTION

The RMX_5 (R=rare earths, M=Co, Rh, Ir, and X=In, Ga) series exhibits a variety of fascinating physical phenomena, which include unconventional superconductivity that coexists with magnetism, complex magnetic order, and multiple quantum phase transitions upon tuning with different parameters [1–4]. Among these, $CeRhIn_5$ exhibits antiferromagnetic ordering below $T_N = 3.8$ K, and complex behaviors emerge in applied magnetic fields with multiple magnetic phases, as well as a Fermi surface reconstruction, enhanced hybridization, and spin nematicity [3,5–11]. $CeRhIn_5$ also exhibits pressure-induced superconductivity, with T_c reaching 2.1 K at 2.1 GPa [12], while $CeCoIn_5$ [13] and $CeIrIn_5$ [14] are heavy fermion superconductors at ambient pressure, with superconducting transition temperatures $T_{sc} = 2.3$ K and 0.4 K, respectively. On other hand, among the isostructural gallides, $PuCoGa_5$ and $PuRhGa_5$ are also unconventional superconductors at ambient pressure, with $T_{sc} = 18.5$ K [15] and 8.7 K, respectively, which are proposed to be d wave superconductors with T_{sc} exceeding those of other heavy fermion superconductors [16,17]. The unusual magnetic properties observed for RMX_5, which are, in part, driven by the quasi-two-dimensional layered crystal structure, are central for realizing novel behaviors such as heavy fermion superconductivity, spin nematicity, unconventional quantum criticality, and complex magnetism [2,4,5,9,15].

Most studies of the RMX_5 series have focused on the Ce- and Pu-based compounds, although even in the absence of f electrons $LaRhIn_5$ exhibits a topological band structure with Dirac fermions [18]. As such, further studies investigating the role played by f electrons in the unusual properties of RMX_5 and their evolution upon tuning with pressure and magnetic fields are important.

In the case of $RMGa_5$, complex magnetic ground states are observed upon the substitution of other rare-earth elements. $TbCoGa_5$ exhibits successive antiferromagnetic transitions with $T_{N1} = 36.2$ K and $T_{N2} = 5.4$ K, which are proposed to be component-separated magnetic transitions where the c component of the Tb^{3+} moment orders antiferromagnetically below T_{N1}, whereas the in-plane component remains paramagnetic, ordering only at T_{N2} [19,20]. $HoCoGa_5$ hosts incommensurate antiferromagnetic order below $T_{N1} = 9.6$ K which becomes commensurate below $T_{N2} = 7.5$ K [21], while $ErCoGa_5$, $TmCoGa_5$, and $YbCoGa_5$ show no sign of magnetic order down to 2 K [22,23].

$DyCoGa_5$ is a little-studied member of this series that is reported to crystallize in a layered tetragonal structure and exhibits antiferromagnetic order with $T_N = 25$ K [22]. In this paper, we report a detailed investigation of the structural and magnetic properties of $DyCoGa_5$, which are investigated using single-crystal x-ray diffraction (XRD), magnetic susceptibility, specific heat, and electrical resistivity measurements. We find that $DyCoGa_5$ crystallizes in a quasi-two-dimensional tetragonal structure with $c/a \approx 1.61$ and undergoes two successive antiferromagnetic transitions at $T_{N1} = 24.7$ K and $T_{N2} = 22.9$ K. When magnetic fields are applied, highly anisotropic magnetic behaviors are observed, as evidenced by strong easy-axis anisotropy with

*yjzhang@hbnu.edu.cn
†msmidman@zju.edu.cn
‡hqyuan@zju.edu.cn

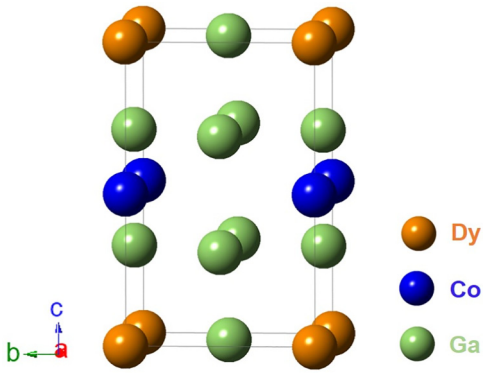

FIG. 1. Crystal structure of $DyCoGa_5$, where orange, green, and blue represent the Dy, Ga, and Co atoms, respectively.

very different T-H phase diagrams for $H \parallel c$ and $H \parallel ab$. T_{N1} and T_{N2} are suppressed by magnetic fields, and multiple metamagnetic transitions are observed for $H \parallel c$, leading to a complex temperature-field diagram for this field direction. These behaviors are in line with the multiple field-induced magnetic phases observed in $CeRhIn_5$, which appear to arise from the complex interplay of physical factors such as crystalline-electric-field effects, quasi-two-dimensionality, and anisotropic magnetic exchange interactions.

II. EXPERIMENTAL DETAILS

Single crystals of $DyCoGa_5$ were grown using a gallium flux. Dy ingots, Co powder, and Ga ingots were placed in an alumina crucible in a 1:1:40 atomic ratio and sealed in an evacuated quartz tube. The tube was heated up to 1050 °C and held at this temperature for 20 h, before being cooled slowly to 500 °C and centrifuged to remove excess Ga. Shiny cuboidlike single crystals, with lengths of 2–5 mm, were obtained, and the phase was determined to be $DyCoGa_5$ using single-crystal XRD and energy-dispersive x-ray spectroscopy. Single crystals of $LuCoGa_5$, which were used as a nonmagnetic analog, were grown using an analogous method. The structure was determined by using a Bruker diffractometer with an x-ray wavelength of $\lambda = 0.71073$ Å. The magnetic susceptibility, heat capacity, and electrical resistivity were all measured using a Quantum Design physical property measurement system (PPMS-9 T) including a vibrating sample magnetometer option.

III. RESULTS

A. Crystal structure

$DyCoGa_5$ crystallizes in the tetragonal $HoCoGa_5$-type structure with space group $P4/mmm$, as displayed in Fig. 1. The crystal structure was confirmed using single-crystal XRD, and the refinement results are shown in Table I, where the refined lattice parameters at 300 K are $a = 4.1983(2)$ Å and $c = 6.7668(6)$ Å, which are consistent with a previous report [22]. The nearest-neighbor Dy-Dy distances in the ab plane are about 4.1983 Å, which is smaller than the value of 6.7668 Å along the c axis, indicating a quasi-two-dimensional structural characteristic of $DyCoGa_5$.

TABLE I. Results from refining single-crystal XRD measurements of $DyCoGa_5$, where the refinement parameters R_1 and wR_2, atomic coordinates, and isotropic displacement parameters U_{eq} are displayed.

Parameter		Value		
Formula		$DyCoGa_5$		
Space group		$P4/mmm$ (No. 123)		
Lattice parameters		$a = 4.1983(2)$ Å, $c = 6.7668(6)$ Å		
R_1, wR_2		0.0260, 0.0577		
Atom	x	y	z	U_{eq}
Dy1	1.00	1.00	1.00	0.0074(4)
Ga2	0.50	0.50	1.00	0.0101(5)
Ga1	1.00	0.50	0.69011(15)	0.0102(4)
Co1	1.00	0.00	0.50	0.0080(4)

B. Antiferromagnetic transitions in $DyCoGa_5$

Figure 2 shows the temperature dependence of the magnetic susceptibility and inverse magnetic susceptibility of $DyCoGa_5$ measured in a field of $\mu_0 H = 0.1$ T for $H \parallel c$ and $H \parallel ab$. The low-temperature $\chi(T)$ for $H \parallel c$ and $H \parallel ab$ both show a peak at the antiferromagnetic ordering temperature $T_{N1} = 24.7$ K, which is consistent with previous reports [22]. As displayed in Fig. 2(a), there is another drop at lower temperatures at $T_{N2} = 22.9$ K, corresponding to an additional antiferromagnetic transition. The value of χ for $H \parallel c$ is

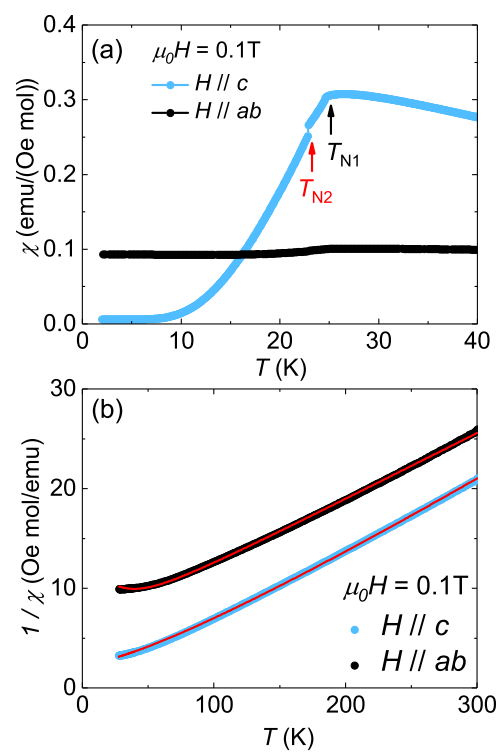

FIG. 2. (a) The low-temperature magnetic susceptibility $\chi(T)$ of $DyCoGa_5$ measured in an applied field of 0.1 T both parallel to the c axis and in the ab plane. (b) Temperature dependence of $1/\chi$ up to 300 K for the two field directions, where the solid lines show the results from fitting with the CEF model described in the text.

higher than that for $H \parallel ab$, indicating that the c axis is the easy axis of magnetization.

At higher temperatures, the data for both field directions above 50 K can be analyzed using a modified Curie-Weiss law: $\chi = \chi_0 + C/(T - \theta_P)$, where χ_0 is the temperature-independent term, C is the Curie constant, and θ_P is the Curie-Weiss temperature. The corresponding effective moments from the Curie-Weiss fitting are $10.62\mu_B$/Dy with a θ_P of 5.7 K for $H \parallel c$, while the respective values are $10.82\mu_B$/Dy and -79.8 K for $H \parallel ab$, where the effective moments are both close to the expected value of $10.63\mu_B$ for the $J = \frac{15}{2}$ multiplet of Dy^{3+}. At lower temperatures, $\chi(T)$ deviates from Curie-Weiss behavior, which arises from the splitting of the ground state multiplet by the crystalline electric field (CEF). The Hamiltonian for a Dy^{3+} ion in a tetragonal CEF is given by [24]

$$H_{\mathrm{CEF}} = B_2^0 O_2^0 + B_4^0 O_4^0 + B_4^4 O_4^4 + B_6^0 O_6^0 + B_6^4 O_6^4, \quad (1)$$

where B_l^m are the Stevens coefficients and O_l^m are the Stevens operator equivalents. Assuming isotropic Heisenberg magnetic exchange interactions, B_2^0 can be calculated using [25,26]

$$B_2^0 = \frac{10k_B\left(\theta_P^{ab} - \theta_P^c\right)}{3(2J-1)(2J+3)}, \quad (2)$$

where θ_P^{ab} and θ_P^c are the Curie-Weiss temperatures in the ab plane and along the c axis, respectively, which yields $B_2^0 = -0.09746$ meV. Keeping B_2^0 from Eq. (2) fixed, the CEF scheme was analyzed by fitting the magnetic susceptibility χ^i together with the magnetic specific heat C_m above T_{N1} (see below) using the following expressions:

$$\chi^i = \chi_0^i + \frac{\chi_{\mathrm{CEF}}^i}{1 - \lambda^i \chi_{\mathrm{CEF}}^i}, \quad (3)$$

$$C_m = \frac{\partial}{\partial T}\left[\frac{1}{Z}\sum_n E_n \exp\left(-\frac{E_n}{k_B T}\right)\right], \quad (4)$$

where χ_0^i is the temperature-independent contribution along the i direction, χ_{CEF}^i is the corresponding CEF susceptibility, λ^i are the molecular field parameters, and E_n is the energy splitting of the nth CEF level. The fitted results are shown by the solid lines in Figs. 2(b) and 3(b), yielding $B_4^0 = 1.77 \times 10^{-4}$ meV, $B_4^4 = 0.0015$ meV, $B_6^0 = -4.77 \times 10^{-6}$ meV, $B_6^4 = 4.73 \times 10^{-5}$ meV, $\lambda^c = -2.12$ mol/emu, $\lambda^{ab} = -2.76$ mol/emu, $\chi_0^c = -2.4 \times 10^{-3}$ emu/mol, and $\chi_0^{ab} = 1.0 \times 10^{-3}$ emu/mol. These parameters give rise to a ground state Kramers doublet wave function $|\psi_1^{\pm}\rangle = 0.866|\pm\frac{15}{2}\rangle + 0.0005|\mp\frac{9}{2}\rangle - 0.500|\pm\frac{7}{2}\rangle - 0.0014|\mp\frac{1}{2}\rangle$, with the first excited doublet situated at $\Delta_1 = 8.24$ meV. Note that this CEF level scheme with a negative B_2^0 gives rise to the pronounced Ising anisotropy with an easy c axis.

The temperature dependence of the magnetic contribution to the specific heat C_m of $DyCoGa_5$ is shown for low temperatures in Fig. 3(a), where C_m is obtained by subtracting the total specific heat of nonmagnetic isostructural $LuCoGa_5$. The total specific heats of $DyCoGa_5$ and $LuCoGa_5$ are displayed in the inset, where the data for $LuCoGa_5$ and $DyCoGa_5$ almost overlap above 120 K, indicating that these compounds have similar lattice contributions. Two consecutive sharp jumps in

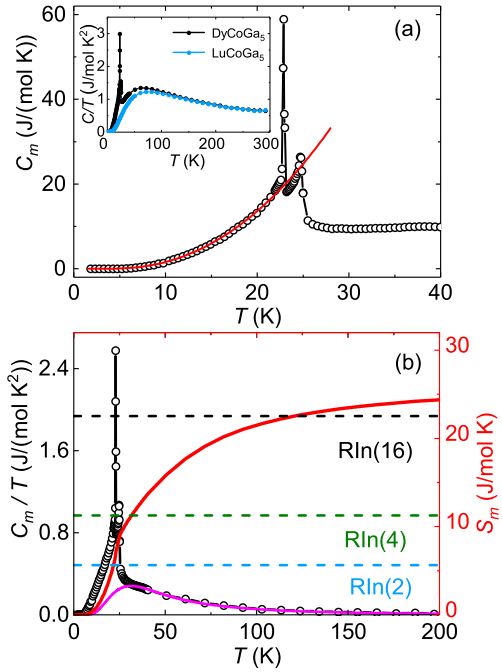

FIG. 3. (a) Temperature dependence of the magnetic specific heat C_m of $DyCoGa_5$ at low temperatures, obtained from subtracting an estimate of the lattice contribution from $LuCoGa_5$. The red solid line shows the results from fitting with Eq. (5). The inset displays the total specific heat C/T of $DyCoGa_5$ (black) and the nonmagnetic analog $LuCoGa_5$ (blue). (b) Temperature dependence of C_m/T and the magnetic entropy S_m of $DyCoGa_5$, where the magenta solid line shows the specific heat calculated from the CEF model described in the text.

C_m occur at $T_{N1} = 24.7$ K and $T_{N2} = 22.7$ K, which are highly consistent with the two transitions observed in $\chi(T)$. The specific heat of $LuCoGa_5$ below 7 K was fitted using $C/T = \gamma + \beta T^2$, giving rise to a Sommerfeld coefficient $\gamma = 5.81(5)$ mJ/mol K^2, a phonon contribution of $\beta = 0.352(2)$ mJ/mol K^4, and a Debye temperature $\Theta_D = 337.9$ K. As shown in Fig. 3(a), the data for $DyCoGa_5$ below T_{N2} can well described by

$$C_m = \gamma' T + c\Delta_{\mathrm{SW}}^{7/2}\sqrt{T}\exp\left(-\frac{\Delta_{\mathrm{SW}}}{T}\right) \times \left[1 + \frac{39}{20}\frac{T}{\Delta_{\mathrm{SW}}} + \frac{51}{32}\left(\frac{T}{\Delta_{\mathrm{SW}}}\right)^2\right], \quad (5)$$

where the first term corresponds to the electronic contribution and the second term arises from antiferromagnetic spin-wave excitations with a spin-wave gap Δ_{SW} [27]. The fitted parameters are $\gamma' = 0.24(5)$ mJ/mol K^2, $\Delta_{\mathrm{SW}} = 24.5(7)$ K, and $c = 0.039(2)$ mJ/mol^2. The very small γ' corresponds to a small difference between the Sommerfeld coefficients of $DyCoGa_5$ and $LuCoGa_5$, indicating that the $4f$ electrons of $DyCoGa_5$ are well localized. The sizable value of Δ_{SW} relative to T_N is consistent with the strong Ising magnetocrystalline anisotropy in $DyCoGa_5$.

The temperature dependence of C_m/T and the magnetic entropy S_m of $DyCoGa_5$ at elevated temperatures are displayed in Fig. 3(b), where S_m was obtained by integrating C_m/T. The

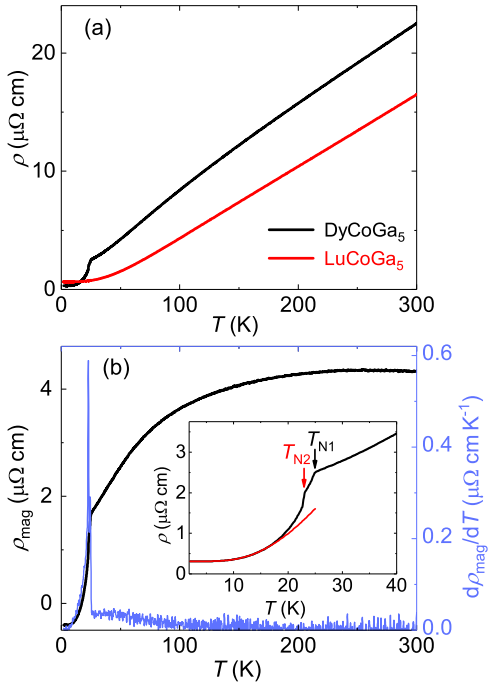

FIG. 4. Temperature dependence of the resistivity $\rho(T)$ of $DyCoGa_5$ and $LuCoGa_5$, measured with the current in the *ab* plane. (b) Temperature dependence of the magnetic contribution to the resistivity ρ_{mag} and the corresponding derivative $d\rho_{mag}/dT$ of $DyCoGa_5$, where ρ_{mag} was obtained from subtracting the $LuCoGa_5$ data, after scaling the $LuCoGa_5$ data so that the slope of the high temperature $\rho(T)$ was the same as that of $DyCoGa_5$. The inset shows the low-temperature $\rho(T)$ of $DyCoGa_5$, where the arrows correspond to the antiferromagnetic transitions T_{N1} and T_{N2}. The red line shows the result from fitting the data in the AFM state using Eq. (6).

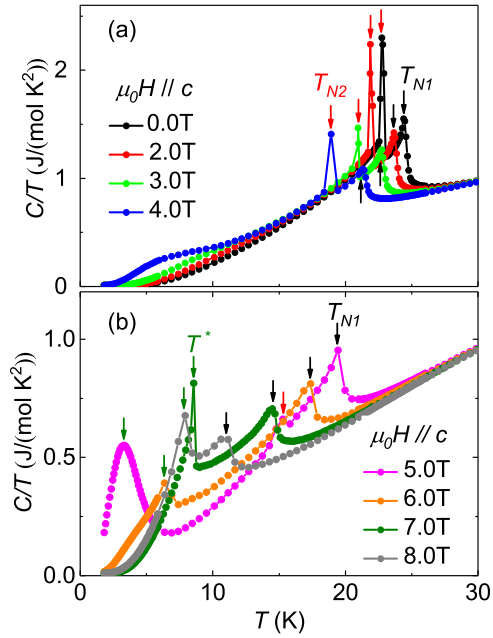

FIG. 5. Temperature dependence of C/T of $DyCoGa_5$ measured in (a) zero field and various fields applied along the *c* axis below 5 T and (b) fields applied along the *c* axis beyond 5 T. The black, red, and olive arrows correspond to the transitions at T_{N1}, T_{N2}, and T^*, respectively.

solid magenta line shows the calculated contribution from the fitted CEF model, suggesting that C_m/T above T_{N1} are mainly accounted for by the excited CEF. The magnetic entropies S_m released at T_{N2} and T_{N1} are around 63% and 76% of $R\ln 4$, respectively, which are higher than the value of $R\ln 2$ expected for a doublet ground state, in line with a significant contribution from excited CEF levels to the low-temperature properties. The high-temperature S_m is close to the expected $R\ln(16)$ for the full $J = 15/2$ multiplet.

The temperature dependence of the resistivity $\rho(T)$ of $DyCoGa_5$ and nonmagnetic isostructural $LuCoGa_5$ are displayed in Fig. 4(a), measured with the current applied in the *ab* plane. In both compounds, $\rho(T)$ decreases with decreasing temperature, corresponding to metallic behavior, where the nearly linear behavior at high temperatures is ascribed to electron-phonon coupling. The residual resistivity ρ_0 and residual resistivity ratio [$= \rho(300\text{ K})/\rho(2\text{ K})$] of $DyCoGa_5$ are around 0.31 μΩ cm and 72, respectively. The magnetic contribution ρ_{mag} of $DyCoGa_5$ is shown in Fig. 4(b), which is obtained from subtracting the data for $LuCoGa_5$ that were scaled so that the slope of the resistivity at high temperatures was the same as that of $DyCoGa_5$. ρ_{mag} shows only a weak temperature dependence above 150 K, where the entropy derived from C_m/T is close to the full multiplet value, but there is a more pronounced decrease below around 100 K due to CEF effects. This can be seen from the plotted $d\rho_{mag}/dT$, which exhibits a broad hump in the paramagnetic state similar to that observed in C_m/T [Fig. 3(b)], which was ascribed to the contribution from excited CEF levels. As shown in the inset, two well-pronounced slope changes are observed at low temperatures at $T_{N1} = 24.7$ K and $T_{N2} = 22.7$ K, corresponding to the two transitions observed in $\chi(T)$ and $C(T)$. $\rho(T)$ of $DyCoGa_5$ below T_N was analyzed using [28,29],

$$\rho(T) = \rho_0 + AT^2 + b\Delta^2\sqrt{\frac{T}{\Delta}}\exp\left(-\frac{\Delta}{T}\right) \times \left[1 + \frac{2}{3}\frac{T}{\Delta} + \frac{2}{15}\left(\frac{T}{\Delta}\right)^2\right], \quad (6)$$

where the second term corresponds to the Fermi-liquid contribution and the third term arises due to scattering by antiferromagnetic spin-wave excitations with a spin-wave gap Δ. The results from fitting the zero-field data below $0.65T_N$ are displayed in the inset of Fig. 4(b), yielding $\rho_0 = 0.31(1)$ μΩ cm, $A = 0.00011(3)$ μΩ cm K^{-2}, $b = 0.0042(6)$ μΩ cm K^{-4}, and $\Delta = 48(1)$ K. The different values of Δ from the analysis of $\rho(T)$ and C_m data may reflect the simplified nature of the utilized spin-wave models.

C. Temperature-magnetic field phase diagrams

The temperature dependence of C/T in various fields for $H \parallel c$ is displayed in Fig. 5. $C(T)/T$ exhibits a λ-type peak at T_{N1} and a δ-type jump at T_{N2} at low fields, as marked by the arrows in Fig. 5(a). Both the anomalies at T_{N1} and T_{N2} gradually shift to lower temperatures with increasing magnetic field for $\mu_0 H \leqslant 4$ T, as expected for antiferromagnetic transitions.

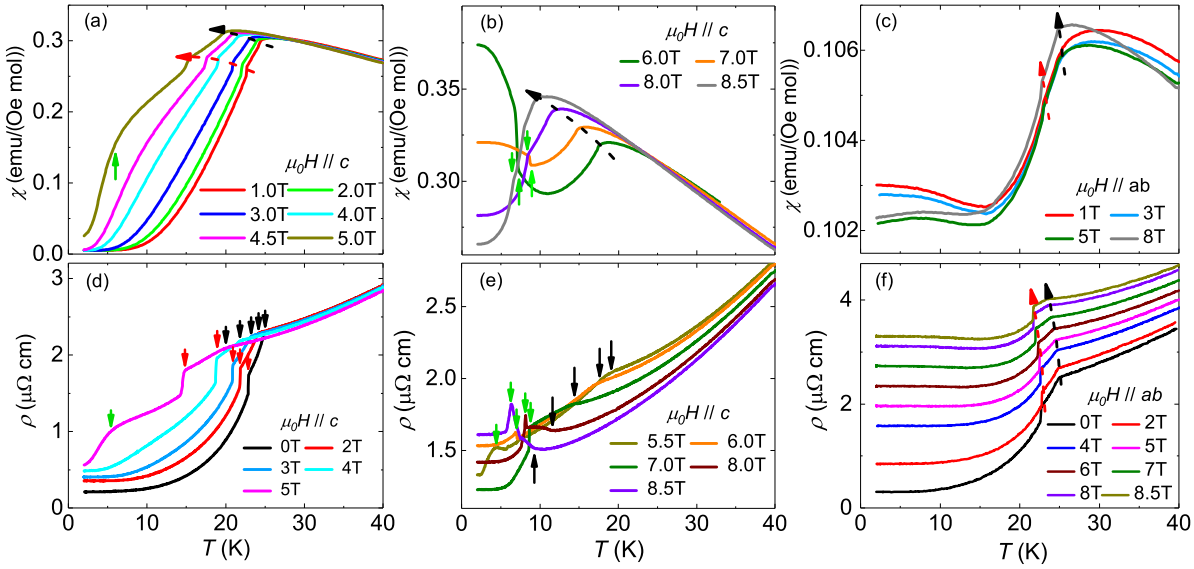

FIG. 6. (a)–(c) $\chi(T)$ of $DyCoGa_5$ measured with various fields applied along the c axis and in the ab plane. (d)–(f) $\rho(T)$ of $DyCoGa_5$ in various fields applied parallel to the c axis and ab plane, with the current in the ab plane. The black, red, and green arrows correspond to the transitions at T_{N1}, T_{N2}, and T^*, respectively.

In a field of 5 T, in addition to the two antiferromagnetic transitions at 19.4 and 15.3 K, a new magnetic transition denoted T^* is observed, for which there is a peak in $C(T)/T$ at 3.4 K, as shown in Fig. 5(b). Above 5 T, the transition T_{N2} is no longer observed, and T^* shows a nonmonotonic field dependence, shifting first to higher temperatures with field up to 7 T and then to lower temperatures upon further increasing the field.

Figures 6(a) and 6(b) show $\chi(T)$ for various fields applied along the c axis. The two magnetic phase transitions T_{N1} and T_{N2} marked by the arrows in Fig. 6(a) are gradually suppressed to lower temperatures with increasing magnetic field. As shown in Fig. 6(b), in a field of 6 T the transition corresponding to T_{N2} disappears, and instead of a drop in $\chi(T)$, there is an upturn corresponding to the field-induced transition T^*. With further increasing field, T^* shifts first to higher temperatures and then to lower temperatures. Meanwhile, the abrupt increase in $\chi(T)$ below T^* is suppressed with increasing field, and a drop reappears in $\chi(T)$ for $\mu_0 H \geqslant 8$ T.

$\rho(T)$ of $DyCoGa_5$ for various fields applied parallel to the c axis are shown in Figs. 6(d) and 6(e), with the current in the ab plane. At low fields, two anomalies are observed in $\rho(T)$ [Fig. 6(d)], corresponding to the antiferromagnetic transitions T_{N1} and T_{N2}, and the two transitions are slowly suppressed to lower temperatures with increasing field. At 5 T, in addition to the anomalies at T_{N1} and T_{N2}, a broad shoulder is observed below T_{N1}, which may correspond to the field-induced magnetic transition T^*. At higher fields, an abrupt jump appears in $\rho(T)$, as displayed in Fig. 6(e), and the field dependence of the anomaly is consistent with that found in the specific heat and magnetic susceptibility measurements, which is ascribed to the field-induced magnetic transition.

The temperature dependence of $\chi(T)$ and $\rho(T)$ of $DyCoGa_5$ is displayed in Figs. 6(c) and 6(f) for various fields applied within the ab plane. For $H \parallel ab$, the anomalies corresponding to T_{N1} and T_{N2} are clearly observed, as marked by the arrows. Both T_{N1} and T_{N2} display a weak field dependence in fields up to at least 8 T. This is in line with the ab plane being the hard direction of magnetization.

The isothermal magnetization $M(H)$ and field dependence of the resistivity $\rho(H)$ at different temperatures are displayed in Fig. 7 for fields applied along the c axis and ab plane. As displayed in Fig. 7(a), the magnetization for $H \parallel c$ at 2.0 K undergoes two metamagnetic transitions at $B_1 = 5.4$ T and $B_2 = 5.7$ T. At B_2 the magnetization reaches about $4.60\mu_B$/Dy, which is close to half of the maximum value for Dy^{3+} of $g_J J = 10\mu_B$, where g_J is the Landé g factor and J is the total angular momentum. As the temperature is increased, the metamagnetic transitions become less sharp, B_2 shifts to higher fields, and an additional metamagnetic transition, B_3, is observed at around 8.3 T. Above 10 K but below 25 K, only one weak kink, labeled B_1, can be found in $M(H)$, and it shifts to lower fields with increasing temperatures. For $T \geqslant 25$ K, $M(H)$ shows a linear field dependence with no detectable anomaly, which is consistent with the system being in the paramagnetic state.

All these transitions can also be observed in the isothermal $\rho(H)$ for fields parallel to the c axis, as displayed in Figs. 7(e)–7(g). At 2 K, two anomalies are observed, corresponding to B_1 and B_2, where a sharp jump and drop are observed in $\rho(H)$, and there is little change in the field dependence of $\rho(H)$ for $B_1 < B < B_2$. At $T \leqslant 8$ K, B_1 shows a weak temperature dependence, while B_2 shifts to higher fields with increasing temperatures, and there is a new metamagnetic transition corresponding to B_3 at 7 and 8 K. At $10 \leqslant T < 25$ K, the only pronounced jump in $\rho(H)$ corresponds to B_1, and it shifts to lower fields with increasing temperature and disappears for $T \geqslant 25$ K. At higher fields, there is a decrease in $\rho(H)$, which is consistent with the reduced spin-flip scattering arising from the moments being spin polarized.

As displayed in Fig. 7(d), no transition is observed in the isothermal $M(H)$ for $H \parallel ab$ at any of the measured

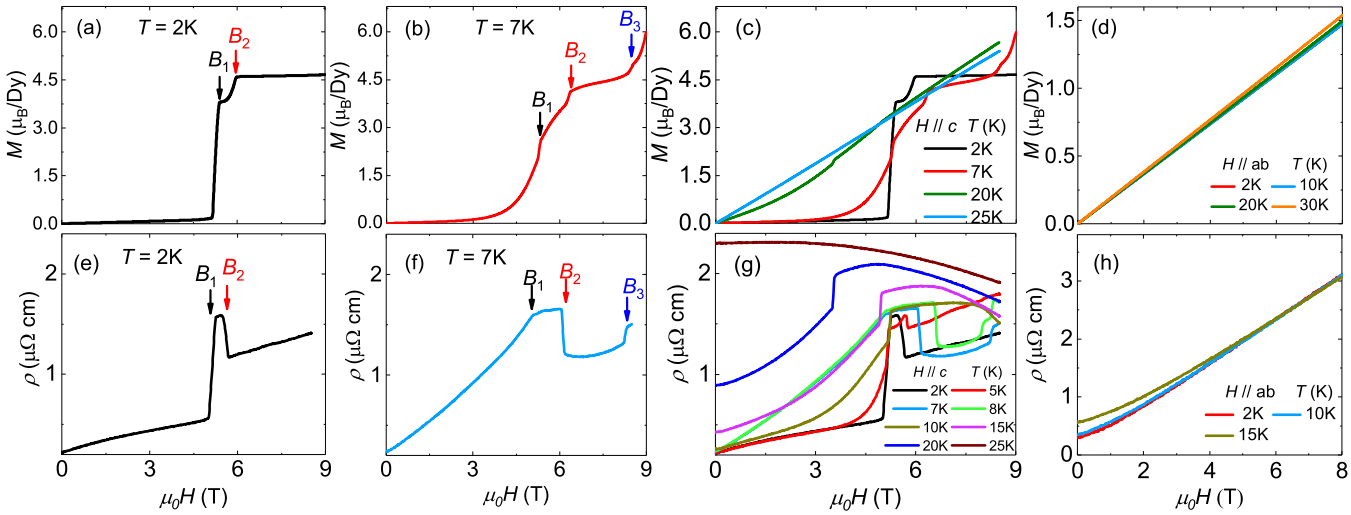

FIG. 7. Field dependence of the magnetization $M(H)$ with $H \parallel c$ at (a) 2 K and (b) 7 K, where the arrows indicate the metamagnetic transitions B_1, B_2, and B_3. The isothermal $M(H)$ at various temperatures for fields applied parallel to the (c) c axis and (d) ab plane. Field dependence of the resistivity $\rho(H)$ with $H \parallel c$ at (e) 2 K and (f) 7 K, measured with the current in the ab plane. The arrows correspond to the metamagnetic transitions observed in $M(H)$. The isothermal $\rho(H)$ are displayed at various temperatures for (g) $H \parallel c$ and (h) $H \parallel ab$.

temperatures. These are consistent with the ab plane being a hard plane of magnetization, where the magnetization for $H \parallel ab$ reaches $1.40\mu_B$/Dy at 8 T and 2 K, compared to $4.64\mu_B$/Dy for $H \parallel c$. As shown in Fig. 7(h), a positive magnetoresistance is observed in $\rho(H)$ for $H \parallel ab$ with no anomalies, while multiple metamagnetic transitions and a

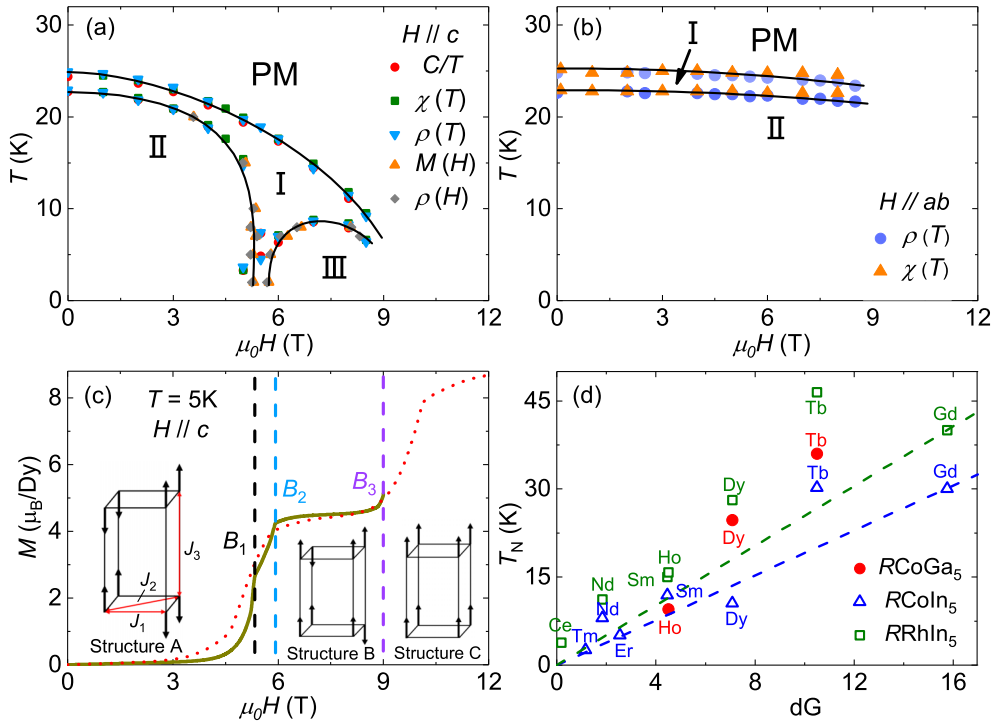

FIG. 8. Temperature-field phase diagrams of $DyCoGa_5$ for magnetic fields applied (a) along the c axis and (b) within the ab plane based on specific heat, susceptibility, resistivity, magnetoresistivity, and magnetization measurements. (c) Field dependence of the magnetization $M(H)$ of $DyCoGa_5$ at 5 K for $H \parallel c$. J_1 and J_2 represent magnetic exchange interactions between nearest-neighbor and next-nearest-neighbor Dy atoms within the ab plane, and J_3 is between nearest-neighboring layers. The red dotted line shows $M(H)$ calculated from the mean-field model described in the text. The insets shows the proposed magnetic structures A, B, and C corresponding to phases II, III, and forced ferromagnetic states of $DyCoGa_5$. (d) Scaling of the antiferromagnetic ordering temperatures of the RCoGa$_5$, RCoIn$_5$, and RRhIn$_5$ series [22,30–34] with the de Gennes factor $(g_J - 1)^2 J(J+1)$, where the dashed lines are guidelines for de Gennes scaling normalized by T_M of the corresponding Gd analogs. The solid circles, open triangles, and open squares display the transition temperatures of RCoGa$_5$, RCoIn$_5$, and RRhIn$_5$, respectively.

negative magnetoresistance are observed in $\rho(H)$ for $H \parallel c$ in the antiferromagnetic state. This angular dependence of the magnetoresistance is a consequence of the strong Ising anisotropy of the Dy moments.

Based on all our results, the T-H phase diagrams for $DyCoGa_5$ for the two field directions are displayed in Figs. 8(a) and 8(b). For $H \parallel c$, three distinct magnetic phases labeled I, II, and III are observed, where phases I and II correspond to the antiferromagnetic phases below T_{N1} and T_{N2} respectively, and the field-induced magnetic phase below T^* is denoted as III. The anomalies at B_1, B_2, and B_3 observed in $M(H)$ and $\rho(H)$ coincide with the boundaries for the three phases. B_1 corresponds to the metamagnetic transition between phases I and II, while the dome-shaped phase III is surrounded by phase I, separated by metamagnetic transitions B_2 and B_3. For $H \parallel ab$, the phase boundaries deduced from $\rho(T)$ and $\chi(T)$ are all consistent, where T_{N1} and T_{N2} exhibit a weak dependence on in-plane fields, as expected for fields applied along the hard magnetization direction.

IV. DISCUSSION

$DyCoGa_5$ exhibits complex magnetism, where in zero field there are two successive magnetic transitions at $T_{N1} = 24.7$ K and $T_{N2} = 22.9$ K, and there are multiple metamagnetic transitions when fields are applied along the c axis. These are shown by the T-B phase diagram in Fig. 8(a), as well as $M(H)$ at 5 K for $H \parallel c$ in Fig. 8(c). Here, B_1 separates magnetic phases II and I, and B_2 corresponds to a change from phase I to the field-induced phase III, with a net magnetization around half of the saturated value, while the third transition B_3 is to the spin-polarized state. A simple model for such a system consists of a square lattice of Dy^{3+} moments with nearest- and next-nearest-neighbor in-plane Heisenberg exchange interactions J_1 and J_2, as well as an interlayer interaction J_3, as illustrated in the inset in Fig. 8(c). Such a model was applied to the isostructural magnetic systems RRhIn$_5$ and TbCoGa$_5$ [35,36].

To analyze the magnetization process, we performed mean-field calculations of the magnetic ground state and magnetization using the MCPHASE software [37], considering both the Heisenberg exchange interactions described above and the CEF Hamiltonian H_{CEF} in Eq. (1). Fixing the Stevens parameters to those obtained from fitting the magnetic susceptibility and magnetic specific heat in the paramagnetic state, we find that $M(H)$ at 5 K are well reproduced by mean-field calculations at this temperature with $J_1 = -0.014$ meV and $2J_2 + J_3 = -0.029$ meV, as plotted with a dotted line in Fig. 8(c). Note that when fixing J_1 and $J_2 + J_3/2$, similar results are obtained for different J_2 and J_3, in line with previous analyses of the metamagnetic transitions of RRhIn$_5$ and TbCoGa$_5$ [35,36]. As such, we cannot uniquely identify the value of J_1/J_2 and hence the degree of in-plane frustration. Such a mean-field model with these parameters predicts magnetic ordering below $T_N^{\mathrm{MF}} = 28$ K, which is slightly larger than the observed $T_{N1} = 24.7$ K. Compared to the previous analysis of TbCoGa$_5$ [36], our model has a relatively larger J_1 compared to $2J_2 + J_3$, suggesting a stronger in-plane nearest-neighbor interaction for $DyCoGa_5$.

In zero field and lower c axis fields, this model predicts the antiferromagnetic structure A with the commensurate propagation vector $k = (1/2, 0, 1/2)$ shown in Fig. 8(c), which can be ascribed to phase II in the experimental phase diagram. Between 5.7 and 9.0 T, structure B has the lowest energy, for which each square consists of three up spins and one down spin. This gives rise to a magnetization of half the saturated value and corresponds to the experimentally observed phase III. Above 9.0 T, there is another metamagnetic transition to the spin-polarized state (structure C). However, this model also predicts only a single transition in zero field and two metamagnetic transitions at low temperature, and it cannot account for the magnetic phase I. It is possible that this phase at elevated temperatures corresponds to incommensurate antiferromagnetic order, similar to HoCoGa$_5$ [21], and therefore, T_{N2} would be a lock-in transition. Accounting for this additional magnetic phase likely requires taking into account additional long-range exchange interactions.

An intricate arrangement of field-induced magnetic phases is also found in CeRhIn$_5$, where the zero-field incommensurate spin helix structure with propagation vector $k = (0.5, 0.5, 0.297)$ [38] locks into a commensurate collinear structure at $k = (0.5, 0.5, 0.25)$ upon applying ab plane fields at low temperatures [7,39]. This field-induced phase forms a domelike structure similar to that of phase III of $DyCoGa_5$ in Fig. 8(a), whereas at elevated temperatures there is a different in-field phase with an elliptical helix [6,7,40,41]. On the other hand, CeRhIn$_5$ has an easy-plane anisotropy that readily gives rise to the aforementioned incommensurate structures, whereas in $DyCoGa_5$ different magnetic structures that are constrained by the strong uniaxial anisotropy are expected.

The antiferromagnetic ordering temperatures of RCoGa$_5$ for R=Tb, Dy, and Ho are 36.2, 24.7, and 9.6 K [22], respectively. In the absence of any crystal-field effect, it is expected that the magnetic ordering temperatures across a rare earth series would scale with the de Gennes factor $(g_J - 1)^2[J(J+1)]$. The evolution of T_N for the RCoGa$_5$, RCoIn$_5$ [22,30–33], and RRhIn$_5$ [34] series as a function of the de Gennes factor is shown in Fig. 8(d). The dashed lines show the expected de Gennes scaling for RCoIn$_5$ and RRhIn$_5$ normalized to the Gd-based compounds where CEF effects are absent. It can be seen that TbRhIn$_5$, TbCoIn$_5$, and DyRhIn$_5$ all have significantly enhanced T_N relative to this scaling, which may be due to the influence of the CEF and associated Ising anisotropy. These factors may also give rise to a similarly enhanced ordering temperature in $DyCoGa_5$, although reports of T_N for GdCoGa$_5$ as a reference are lacking. Compared to the RRhIn$_5$ series, RCoIn$_5$ and RCoGa$_5$ exhibit lower T_N, which is likely due to a smaller nearest-neighbor interplane magnetic exchange in the Co-based materials [42]. It is of particular interest to reveal the magnetic structure and excitations of both the zero-field and field-induced phases of $DyCoGa_5$ in order to examine the complex interplay of factors such as quasi-two-dimensionality, crystalline-electric-field effects, and magnetic exchange interactions in the RMX_5 series.

V. SUMMARY

In conclusion, we characterized the magnetic properties of the layered compound $DyCoGa_5$ and their evolution upon the application of magnetic fields both parallel and perpendicular

to the c axis. In zero field, two successive antiferromagnetic transitions are found with a second-order transition at $T_{N1} = 24.7$ K and a first-order transition at $T_{N2} = 22.9$ K, which arise from ordering of the localized Dy^{3+} moments. We constructed temperature-field phase diagrams for both field directions, in which strong magnetic anisotropy and complex magnetism are observed. Applying magnetic fields along the c axis leads to a field-induced phase with a magnetization half the saturated value, and this corresponds to a dome-shaped region of the phase diagram. By analyzing the magnetic susceptibility and specific heat, we proposed a CEF scheme that gives rise to the observed Ising anisotropy. We considered a simple model including the fitted CEF Hamiltonian and three Heisenberg antiferromagnetic exchange interactions that can account for the low-temperature magnetic phase II and field-induced phase III, although this model cannot explain phase I at elevated temperatures. To reveal the nature of these phases, measurements such as neutron and x-ray diffraction could be performed.

ACKNOWLEDGMENTS

This work was supported by the National Key R&D Program of China (Grants No. 2022YFA1402200 and No. 2023YFA1406303), the National Natural Science Foundation of China (Grants No. U23A20580, No. 12034017, No. 12174332, No. 12204159, No. 12222410, and No. 12204160), and the Hubei Provincial Natural Science Foundation of China (Grant No. 2021CFB220).

[1] J. S. Kim, J. Alwood, G. R. Stewart, J. L. Sarrao, and J. D. Thompson, Specific heat in high magnetic fields and non-Fermi-liquid behavior in $CeMIn_5$(M = Ir, Co), Phys. Rev. B **64**, 134524 (2001).

[2] T. Park, F. Ronning, H. Q. Yuan, M. B. Salamon, R. Movshovich, and J. D. Thompson, Hidden magnetism and quantum criticality in the heavy fermion superconductor $CeRhIn_5$, Nature (London) **440**, 65 (2006).

[3] L. Jiao, Y. Chen, Y. Kohama, D. Graf, E. D. Bauer, J. Singleton, J. X. Zhu, Z. F. Weng, G. M. Pang, T. Shang, J. l. Zhang, H. O. Lee, T. Park, M. Jaime, J. D. Thompson, F. Steglich, Q. Si, and H. Q. Yuan, Fermi surface reconstruction and multiple quantum phase transitions in the antiferromagnet $CeRhIn_5$, Proc. Natl. Acad. Sci. USA **112**, 673 (2015).

[4] Z. F. Weng, M. Smidman, L. Jiao, X. Lu, and H. Q. Yuan, Multiple quantum phase transitions and superconductivity in Ce-based heavy fermions, Rep. Prog. Phys. **79**, 094503 (2016).

[5] A. L. Cornelius, P. G. Pagliuso, M. F. Hundley, and J. L. Sarrao, Field-induced magnetic transitions in the quasi-two-dimensional heavy-fermion antiferromagnets Ce_nRhIn_{3n+2}(n = 1 or 2), Phys. Rev. B **64**, 144411 (2001).

[6] V. F. Correa, W. E. Okraku, J. B. Betts, A. Migliori, J. L. Sarrao, and A. H. Lacerda, High-magnetic-field thermal expansion and elastic properties of $CeRhIn_5$, Phys. Rev. B **72**, 012407 (2005).

[7] S. Raymond, E. Ressouche, G. Knebel, D. Aoki, and J. Flouquet, Magnetic structure of $CeRhIn_5$ under magnetic field, J. Phys.: Condens. Matter **19**, 242204 (2007).

[8] P. J. W. Moll, B. Zeng, L. Balicas, S. Galeski, F. F. Balakirev, E. D. Bauer, and F. Ronning, Field-induced density wave in the heavy-fermion compound $CeRhIn_5$, Nat. Commun. **6**, 6663 (2015).

[9] F. Ronning, T. Helm, K. R. Shirer, M. D. Bachmann, L. Balicas, M. K. Chan, B. J. Ramshaw, R. D. McDonald, F. F. Balakirev, M. Jaime, E. D. Bauer, and P. J. W. Moll, Electronic in-plane symmetry breaking at field-tuned quantum criticality in $CeRhIn_5$, Nature (London) **548**, 313 (2017).

[10] L. Jiao, M. Smidman, Y. Kohama, Z. S. Wang, D. Graf, Z. F. Weng, Y. J. Zhang, A. Matsuo, E. D. Bauer, H. Lee, S. Kirchner, J. Singleton, K. Kindo, J. Wosnitza, F. Steglich, J. D. Thompson, and H. Q. Yuan, Enhancement of the effective mass at high magnetic fields in $CeRhIn_5$, Phys. Rev. B **99**, 045127 (2019).

[11] P. F. S. Rosa, S. M. Thomas, F. F. Balakirev, E. D. Bauer, R. M. Fernandes, J. D. Thompson, F. Ronning, and M. Jaime, Enhanced hybridization sets the stage for electronic nematicity in $CeRhIn_5$, Phys. Rev. Lett. **122**, 016402 (2019).

[12] H. Hegger, C. Petrovic, E. G. Moshopoulou, M. F. Hundley, J. L. Sarrao, Z. Fisk, and J. D. Thompson, Pressure-induced superconductivity in quasi-2D $CeRhIn_5$, Phys. Rev. Lett. **84**, 4986 (2000).

[13] C Petrovic, P. G. Pagliuso, M. F. Hundley, R. Movshovich, J. L. Sarrao, J. D. Thompson, Z. Fisk, and P. Monthoux, Heavy-fermion superconductivity in $CeCoIn_5$ at 2.3 K, J. Phys.: Condens. Matter **13**, L337 (2001).

[14] C. Petrovic, R. Movshovich, M. Jaime, P. G. Pagliuso, M. F. Hundley, J. L. Sarrao, Z. Fisk, and J. D. Thompson, A new heavy-fermion superconductor $CeIrIn_5$: A relative of the cuprates? Europhys. Lett. **53**, 354 (2001).

[15] J. L. Sarrao, L. A. Morales, J. D. Thompson, B. L. Scott, G. R. Stewart, F. Wastin, J. Rebizant, P. Boulet, E. Colineau, and G. H. Lander, Plutonium-based superconductivity with a transition temperature above 18 K, Nature (London) **420**, 297 (2002).

[16] E. D. Bauer, M. M. Altarawneh, P. H. Tobash, K. Gofryk, O. E. Ayala-Valenzuela, J. N. Mitchell, R. D. McDonald, C. H. Mielke, F. Ronning, J.-C. Griveau, E. Colineau, R. Eloirdi, R. Caciuffo, B. L. Scott, O. Janka, S. M. Kauzlarich, and J. D. Thompson, Localized 5f electrons in superconducting $PuCoIn_5$: Consequences for superconductivity in $PuCoGa_5$, J. Phys.: Condens. Matter **24**, 052206 (2012).

[17] B. J. Ramshaw, A. Shekhter, R. D. McDonald, J. B. Betts, J. N. Mitchell, P. H. Tobash, C. H. Mielke, E. D. Bauer, and A. Migliori, Avoided valence transition in a plutonium superconductor, Proc. Natl. Acad. Sci. USA **112**, 3285 (2015).

[18] C. Guo *et al.*, Temperature dependence of quantum oscillations from non-parabolic dispersions, Nat. Commun. **12**, 6213 (2021).

[19] N. Sanada, T. Muneoka, R. Watanuki, K. Suzuki, M. Akatsu, and T. Sakakibara, Successive component-separated magnetic transition in $TbCoGa_5$, J. Phys.: Conf. Ser. **150**, 042172 (2009).

[20] Y. Tokunaga, Y. Saito, H. Sakai, S. Kambe, N. Sanada, R. Watanuki, K. Suzuki, Y. Kawasaki, and Y. Kishimoto, NMR determination of noncollinear antiferromagnetic structure in $TbCoGa_5$, Phys. Rev. B **84**, 214403 (2011).

[21] R. Kobayashi, K. Kaneko, S. Wakimoto, S. Chi, N. Sanada, R. Watanuki, and K. Suzuki, Powder neutron diffraction study of $HoCoGa_5$, J. Korean Phys. Soc. **63**, 337 (2013).

[22] J. Hudis, R. Hu, C. L. Broholm, V. F. Mitrović, and C. Petrovic, Magnetic and transport properties of $RCoIn_5$ (R=Pr,Nd) and $RCoGa_5$ (R=Tb,Tm), J. Magn. Magn. Mater. **307**, 301 (2006).

[23] E. K. Okudzeto, K. Kuga, S. Nakatsuji, and J. Y. Chan, Crystal growth, transport, and magnetic properties of $YbCoGa_5$, Cryst. Growth Des. **9**, 1956 (2009).

[24] M. T. Hutchings, Point-charge calculations of energy levels of magnetic ions in crystalline electric fields, Solid State Phys. **16**, 227 (1964).

[25] Y.-L. Wang, Crystal-field effects of paramagnetic curie temperature, Phys. Lett. A **35**, 383 (1971).

[26] P. Boutron, Exact calculation of the paramagnetic susceptibility of a single crystal with arbitrary crystal field and exchange interactions, Phys. Rev. B **7**, 3226 (1973).

[27] S. N. de Medeiros, M. A. Continentino, M. T. D. Orlando, M. B. Fontes, E. M. Baggio-Saitovitch, A. Rosch, and A. Eichler, Quantum critical point in $CeCo(Ge_{1-x}Si_x)_3$: Oral presentation, Physica B (Amsterdam, Neth.) **281–282**, 340 (2000).

[28] M. B. Fontes, J. C. Trochez, B. Giordanengo, S. L. Bud'ko, D. R. Sanchez, E. M. Baggio-Saitovitch, and M. A. Continentino, Electron-magnon interaction in RNiBC (R = Er, Ho, Dy, Tb, and Gd) series of compounds based on magnetoresistance measurements, Phys. Rev. B **60**, 6781 (1999).

[29] Y. J. Zhang, B. Shen, F. Du, Y. Chen, J. Y. Liu, H. Lee, M. Smidman, and H. Q. Yuan, Structural and magnetic properties of antiferromagnetic Ce_2IrGa_{12}, Phys. Rev. B **101**, 024421 (2020).

[30] Y. Isikawa, D. Kato, A. Mitsuda, T. Mizushima, and T. Kuwai, Magnetic properties of single crystals of $RCoIn_5$ (R=Tb,Dy,Ho,Er,Yb), J. Magn. Magn. Mater. **272–276**, 635 (2004).

[31] Y. Inada, M. Hedo, T. Fujiwara, T. Sadamasa, and Y. Uwatoko, Physical properties of $SmMIn_5$ (M=Co, Rh, Ir), Physica B (Amsterdam, Neth.) **378–380**, 421 (2006).

[32] D. Betancourth, J. I. Facio, P. Pedrazzini, C. B. R. Jesus, P. G. Pagliuso, V. Vildosola, P. S. Cornaglia, D. J. García, and V. F. Correa, Low-temperature magnetic properties of $GdCoIn_5$, J. Magn. Magn. Mater. **374**, 744 (2015).

[33] H. T. Huy, S. Noguchi, N. Van Hieu, X. Shao, T. Sugimoto, and T. Ishida, Electrical and magnetic properties of $TmCoIn_5$ and $YbCoIn_5$ single crystals, J. Magn. Magn. Mater. **321**, 2425 (2009).

[34] N. V. Hieu, T. Takeuchi, H. Shishido, C. Tonohiro, T. Yamada, H. Nakashima, K. Sugiyama, R. Settai, T. D. Matsuda, Y. Haga, M. Hagiwara, K. Kindo, S. Araki, Y. Nozue, and Y. Ōnuki, Magnetic properties and crystalline electric field scheme in $RRhIn_5$ (R: rare earth), J. Phys. Soc. Jpn. **76**, 064702 (2007).

[35] N. V. Hieu, H. Shishido, T. Takeuchi, A. Thamizhavel, H. Nakashima, K. Sugiyama, R. Settai, T. D. Matsuda, Y. Haga, M. Hagiwara, K. Kindo, and Y. Ōnuki, Unique magnetic properties of $NdRhIn_5$, $TbRhIn_5$, $DyRhIn_5$ and $HoRhIn_5$, J. Phys. Soc. Jpn. **75**, 074708 (2006).

[36] N. Sanada, Y. Amou, R. Watanuki, K. Suzuki, I. Yamamoto, H. Mitamura, T. Sakakibara, M. Akatsu, Y. Nemoto, and T. Goto, Coexistence of Ising and xy spin systems on a single Tb atom in $TbCoGa_5$, J. Phys. Soc. Jpn. **82**, 044713 (2013).

[37] M Rotter, Using McPhase to calculate magnetic phase diagrams of rare earth compounds, J. Magn. Magn. Mater. **272–276**, E481 (2004).

[38] W. Bao, P. G. Pagliuso, J. L. Sarrao, J. D. Thompson, Z. Fisk, J. W. Lynn, and R. W. Erwin, Incommensurate magnetic structure of $CeRhIn_5$, Phys. Rev. B **62**, R14621 (2000).

[39] D. M. Fobes, S. Zhang, S.-Z. Lin, P. Das, N. J. Ghimire, E. D. Bauer, J. D. Thompson, L. W. Harriger, G. Ehlers, A. Podlesnyak, R. I. Bewley, A. Sazonov, V. Hutanu, F. Ronning, C. D. Batista, and M. Janoschek, Tunable emergent heterostructures in a prototypical correlated metal, Nat. Phys. **14**, 456 (2018).

[40] S. Mishra, A. Demuer, D. Aoki, and I. Sheikin, Specific heat of $CeRhIn_5$ in high magnetic fields: Magnetic phase diagram revisited, Phys. Rev. B **103**, 045110 (2021).

[41] S. Mishra, D. Gorbunov, D. J. Campbell, D. LeBoeuf, J. Hornung, J. Klotz, S. Zherlitsyn, H. Harima, J. Wosnitza, D. Aoki, A. McCollam, and I. Sheikin, Origin of the 30 T transition in $CeRhIn_5$ in tilted magnetic fields, Phys. Rev. B **103**, 165124 (2021).

[42] J. I. Facio, D. Betancourth, P. Pedrazzini, V. F. Correa, V. Vildosola, D. J. García, and P. S. Cornaglia, Why the co-based 115 compounds are different: The case study of $GdMIn_5$(M = Co, Rh, Ir), Phys. Rev. B **91**, 014409 (2015).